Steel and Composite Structures, *Vol. 59, No. 5 (2026) 719-740*
https://doi.org/10.12989/scs.2026.59.5.719

Seismic performance evaluation of CFT column structures using CFRP and HCFRP

Young Chan Kim[1,2,3a], Seyed Javad Mortazavi[3b], Jong Wan Hu[*1,3]

[1]*Department of Civil and Environmental Engineering, Incheon National University, Incheon 22012, Republic of Korea*
[2]*Industry-Academic Cooperation Foundation, Incheon National University, Incheon 22012, Republic of Korea*
[3]*Incheon Disaster Prevention Research Center, Incheon National University, Incheon 22012, Republic of Korea*

(Received February 7, 2026, Revised March 31, 2026, Accepted May 11, 2026)

Abstract. Concrete-filled steel tubes (CFSTs) are composite systems applied to earthquake-resistant structures that enhance structural performance such as strength and ductility by combining the confinement effect of steel tubes with the compressive capacity of concrete. However, steel, the primary component of CFST, is susceptible to corrosion when exposed to the external environment over extended periods, which can lead to degradation of structural performance and even structural collapse. To address issues and enhancing the performance of CFST columns, this study conducted a numerical analysis on concrete-filled CFRP tube (CFCT) and concrete-filled hybrid CFRP tube (CFHT) column structures, which replace steel with CFRP. In addition, to evaluate the seismic performance of CFCT and CFHT columns, the results of the numerical analysis were statistically analyzed for roof displacement, inter-story drift ratio, residual inter-story drift ratio, column stress, energy dissipation amount and permanent deformation. Consequently, the CFCT and CFHT column structures exhibited superior seismic performance in evaluation results.

Keywords: cfrp; cft column; frame structure; numerical analysis; seismic performance

1. Introduction

Recently, structures have been increasing in size owing to advancements in the construction industry and growing social demands. However, unexpected external loads, such as earthquakes, can cause severe damage to large structures by compromising critical components such as columns. To enhance structural safety, composite structures that combine different materials to optimize mechanical performance have been increasingly employed. Among these, composite columns are a representative form, offering excellent structural behavior, owing to the synergistic effects of combining concrete and steel. Particularly, concrete-filled steel tube (CFST) columns, where a concrete core is encased by steel tubes, are widely used to meet higher performance requirements of structures [1, 2]. CFST columns offer several advantages, including enhanced compressive and flexural strength, reduced column thickness, and improved ductility and energy

*Corresponding author, Professor, E-mail: e jongp24@inu.ac.kr
[a] Ph.D., E-mail: channy0409@inu.ac.kr
[b] M.S., E-mail: mortazavi@inu.ac.kr

http://www.techno-press.org/scs/5
ISSN: 1229-9367 (Print), 1598-6233 (Online)

absorption capacity. These benefits result from the internal confinement of the concrete by the steel tube and the suppression of the steel buckling by the concrete core. However, despite these advantages, CFST columns exhibit limitations related to the material properties of the steel tube that serves as a covering. CFST columns benefit from enhanced fire resistance owing to their concrete cores; however, the externally exposed steel tubes remain vulnerable to high temperature during fire [3-6]. Additionally, the steel tubes are susceptible to corrosion in hot and humid environments, leading to a reduction in strength and a potential threat to structural safety [7-12]. To address these issues, protective measures such as paint coating and concrete covering encasements are commonly applied; however, these methods do not offer fundamental or long-term solutions [13].

Consequently, recent research has focused on replacing steel with fiber reinforced polymer (FRP), a composite material, to retain the structural configuration of CFST columns while enhancing structural performance and overcoming material limitations. FRP is a composite material widely used as a substitute for steel and other metals across various industries, owing to its superior properties such as high strength, durability, low weight, fire retardancy, and corrosion resistance. Among different types of FRP, carbon fiber reinforced polymer (CFRP) has been extensively studied for applications in the construction field. Numerous studies have investigated the potential of CFRP to enhance the performance of both existing structures and new buildings, particularly focusing on its applicability as a steel replacement in composite columns. The behavior of concrete columns confined with FRP under axial loads has been thoroughly examined through experimental and analytical approaches. Basically, CFT columns reinforced with FRP show results in effectively improved ultimate strength compared to conventional CFST columns [14-16]. In addition, these investigations demonstrated that FRP confinement significantly enhances the ductility and axial strength of these columns, as the FRP functions as a lateral restraint [17-19]. Similarly, studies on concrete-filled FRP tubes with circular cross-sections have reported improvements in ductility and axial strength owing to the confining action of the FRP tubes [20-22]. A typical structural column is subjected to a combination of axial compressive forces, tensile forces, bending moments, shear forces, and torsional moments. Accordingly, the cross-section of the column must be designed to resist the stresses arising from these combined forces. In a CFST column, the steel tube primarily resists tensile stresses, and the concrete core contributes to resisting compressive and shear stresses. When replacing the steel with FRP material, the FRP fibers must be oriented to effectively resist tensile stresses, as concrete possesses inherently low tensile strength. In addition, tensile failure of the FRP and buckling of the internal longitudinal reinforcement occur due to the interaction between the confined concrete core and the external wrapping FRP [23, 24]. Therefore, to ensure structural integrity, the fibers in the FRP tube with high tensile strength should be aligned longitudinally along the axis of the column. This fiber orientation reduces the confinement effect provided to the concrete, but the fibers resist axial and tensile stresses, thereby reinforcing the concrete core [25-27]. To assess the seismic performance of structures incorporating FRP columns, it is essential to employ analytical methods that can accurately capture the behavior of the structural members. Depending on the required level of precision, various modeling techniques are used to simulate the behavior of FRP materials. For structures with numerous members, elastic and linear modeling of FRP is commonly adopted [28, 29]. In such cases, the compressive strength of FRP is often neglected, and the material is treated as brittle, which may lead to significant errors and reduced accuracy in the analysis.

Therefore, to address the limitations of conventional CFST columns and secure excellent seismic performance, this study conducted a numerical analysis to evaluate the field applicability

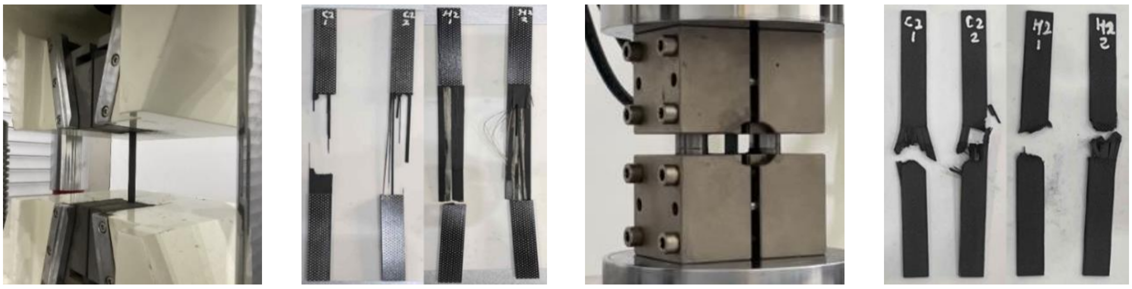

(a) Tensile test and specimen (b) Compressive test and specimen

Figure 1. Tensile and compressive tests and specimens under cyclic loads

and seismic performance of frame structures incorporating concrete-filled CFRP tube (CFCT) and concrete-filled hybrid CFRP tube (CFHT) columns. Initially, the material advantages of CFRP and hybrid CFRP (HCFRP) were validated, and the behavioral characteristics were analyzed based on tensile and compressive test results of CFRP, HCFRP material specimens obtained from a previous study. Based on the test results for each material, the behavioral characteristics were simulated using a newly developed material model implemented in OpenSees. Furthermore, a six-story frame structure incorporating CFCT, CFHT, and CFST columns was designed, and numerical analyses were conducted using 41 ground motion records at two seismic levels: Maximum Considered Earthquake (MCE) and Design Basis Earthquake (DBE). The seismic performance of the frame was then evaluated by examining roof displacement, inter-story drift ratio, residual inter-story drift ratio, column stress, and permanent deformation derived from the numerical analysis results.

2. Simulation of CFRP material behavior characteristics

To evaluate the seismic performance of building structures utilizing CFCT and CFHT columns, the behavioral characteristics of CFRP and HCFRP materials, which are the core materials of this study and constitute the CFCT and CFHT columns, were simulated using a material model. To this end, material test results for the base materials, CFRP and HCFRP, obtained from a previous study, were analyzed [30]. To validate the behavioral characteristics of CFRP and HCFRP and demonstrate their superiority, material tests were conducted on these composites and steel. Specifically, specimens were fabricated using CFRP laminated with carbon-epoxy prepreg UPN116B, HCFRP composed of glass-epoxy prepreg UGN160B integrated into CFRP. HCFRP was selected to complement the brittle fracture characteristics of CFRP. As presented in Fig. 1, for CFRP and HCFRP, tensile and compressive tests under cyclic loads such as earthquakes were performed on 16 specimens each in accordance with ASTM D3039 and ASTM D6641 standards to facilitate their idealization as material models [31, 32]. For the tensile cyclic test, the material test specimens were manufactured with the following specifications: 15 mm in width, 1 mm in thickness, and 318 mm in length. To prevent slippage during testing, tabs measuring 15 mm in width, 1.5 mm in thickness, and 90 mm in length were attached to both ends. For the compressive cyclic test, the material test specimens were also prepared with following specifications: 12 mm in width, 3 mm in thickness, and 140 mm in length. The loading protocol for the tensile cyclic test

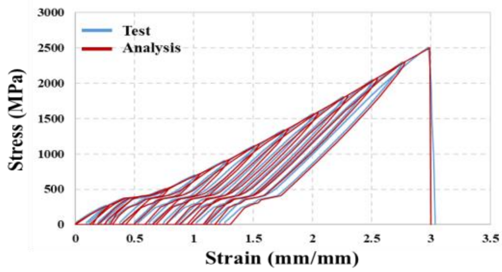

(a) Tensile results of CFRP material

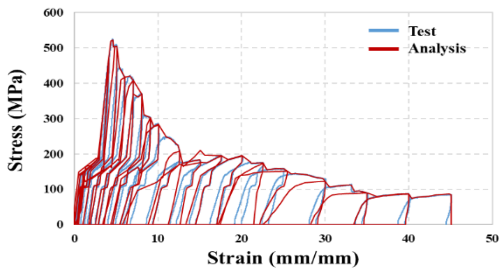

(b) Compressive results of CFRP material

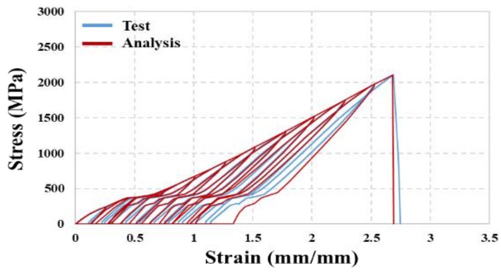

(c) Tensile results of HCFRP material

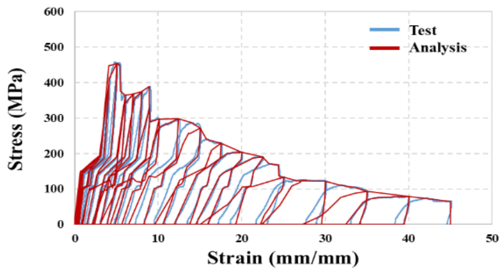

(d) Compressive results of HCFRP material

Figure 2. Comparison of analysis and test results for materials

was displacement-controlled, with a displacement increment of 0.345 mm applied every 20.7 s over a total of 20 cycles. For the compressive cyclic test, displacement control was applied with an increment of 0.127 mm every 7.62 s for a total of 20 cycles. From the stress-strain responses obtained through the tensile and compressive cyclic tests of each material, the maximum tensile strength was recorded as 2511.99 MPa for CFRP and 2089.33 MPa for HCFRP, and the maximum compressive strength was 522.11 MPa for CFRP and 458.89 MPa for HCFRP. Additionally, the numerical analysis was performed using the predefined material model for steel in the OpenSees program.

The numerical analysis of the structure was conducted using the OpenSees program [33]. OpenSees, developed at the University of California, Berkeley, is an open-source software framework based on the object-oriented C++ programming language [34]. This framework has attracted contributions from various researchers to enhance its functionality and become a very efficient and powerful tool for advanced structural analysis [35]. In this study, the behavioral characteristics of CFRP were modeled using a new material class developed by Mortezavi et al., which simulates a newly implemented uniaxial Material class within the OpenSees framework [36]. The material model was constructed using an interpolation method based on the data obtained from tensile and compressive cyclic tests, dividing them into loading and unloading sections so that CFRP and HCFRP materials have their own mechanical properties. Moreover, the setTriaStrain method was employed to define strain values beyond those observed in the tests, enabling the model to return corresponding tangent stiffness and stress values to the analysis program. Here, the material stiffness matrix is derived using the tangent modulus of the material, allowing for the prediction of deformation behavior beyond the scope of the test data. To validate the accuracy of the CFRP and HCFRP material models, a single-column structure with a square cross-section of unit length and unit area was developed using nonlinearbeamcolumn element.

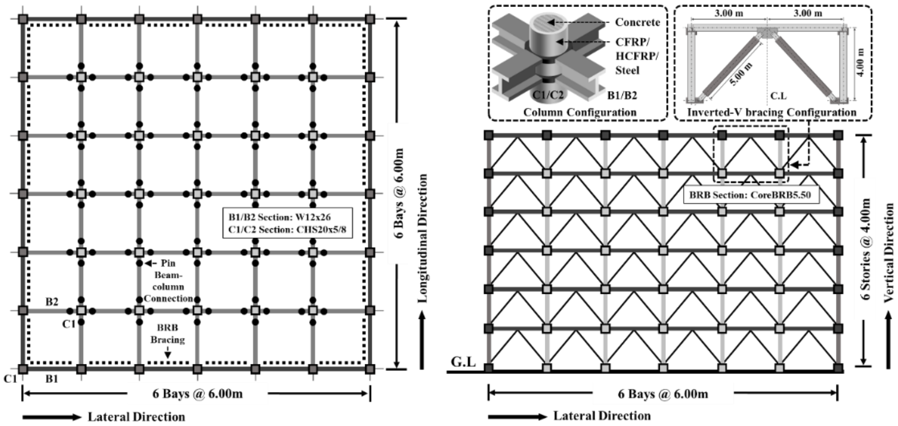

Figure 3. Design of building floor plan and elevation

This model was subjected to axial loading under conditions replicating the test setup. The loading protocol in the OpenSees simulation was designed to precisely match these conditions. Fig. 2 presents a comparison between the analysis and test results for CFRP and HCFRP materials under both tensile and compressive cyclic loading. As shown in Figures, the strong correlation between the analysis result and test result confirms the reliability of the CFRP and HCFRP material models. This close agreement indicates that material properties and behaviors were accurately implemented, verifying the effectiveness of the simulation for CFRP and HCFRP materials. Steel modeling was performed in OpenSees using the uniaxial material `steel02` assigned to the column cross-section.

3. Building structure design

The structure used for numerical analysis was a six-bay, six-story residential building located in Los Angeles, California. Each story was assigned a height of 4 m, and each bay a length of 6 m. The site is characterized by hard clay soil, which influences both the foundation design and overall structural behavior. The floor plan and elevation layout of the building are presented in Fig. 3. The lateral force-resisting system consists of moment-resisting frames and inverted-V-shaped buckling-restrained braces (BRBs) arranged in two main directions to ensure seismic safety. These lateral systems are implemented around the perimeter of the building, whereas the interior structural elements are designed solely to support gravity loads. To reflect this, the connections between beams and columns in the interior frames are modeled as pinned joints, as indicated by the dots on the beams. The roof consists of a flat, 200 mm thick reinforced concrete slab designed to function as a rigid diaphragm to ensure uniform distribution of seismic forces across the structure. The building's beams are W series I sections fabricated from A992 grade steel, and the BRBs are supplied by CoreBrace. The columns are square-shaped CFTs utilizing CFRP, HCFRP, steel and C350 grade concrete to ensure adequate strength and stability. The columns were designed with the same parameters except for the material. The final section sizes for all structural elements were selected in accordance with the design provisions and requirements specified in AISC-341-22 and AISC360-22 [37, 38].

Table 1. Applied loads used in the numerical analysis

Story	Roof Dead Load (kN/m2)	Roof Live load (kN/mm=2)	Exterior Wall Load (KN/m)
1-5	11	0.2	8
6	0.9	0.2	3

Table 2. Seismic load parameters in accordance with ASCE7-22

Parameter	S_s	S_1	T_L	S_{DS}	S_{D1}	R	I	C_d	Ω	ρ
Value	2.32	0.74	8	1.5467	1.1401	8	1	2.5	2.5	1

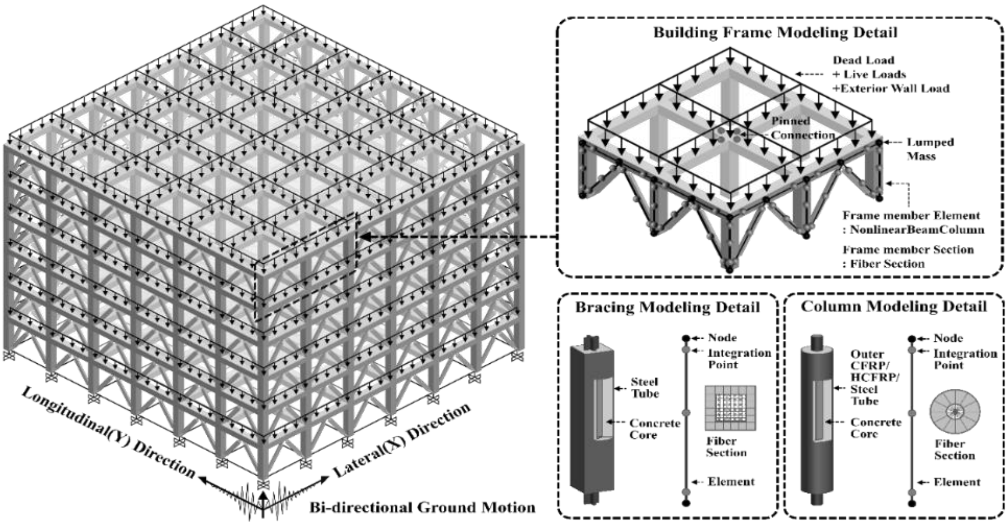

Figure 4. Numerical analysis model of building frame structure

The loads acting on the building were calculated in accordance with provisions of ASCE7-22 [39]. These include dead loads, accounting for the self-weight of the building, and live loads, representing transient occupancy-related loads such as furniture and human activity. Owing to the site's high seismic risk, seismic lateral loads were carefully considered in the structural analysis. Other environmental loads, such as wind, snow, and rain, were deemed negligible based on the local climatic conditions and were therefore excluded from the load combinations. A summary of the estimated structural gravity loads, including both dead and live loads, is provided in Table 1. For seismic loading, the structure is classified as Seismic Design Category E. The seismic design parameters, derived from ASCE7-22, incorporate site-specific seismic activity, soil profile, and the building dynamic characteristics, as summarized in Table 2.

4. Building frame structure analysis model

Three types of frame structures utilizing CFCT, CFHT, and CFST columns were modeled in OpenSees in 3D space, incorporating six degrees of freedom. The primary distinction among these models lies in the material composition of the CFT columns. Each of the column structures

Table 3. Ground motion specifications

ID	RSN30	RSN95	RSN158	RSN159	RSN161	RSN162	RSN165
Earthquake Name	Imperial Valley-02	Parkfield	Managua Nica.-01	Imperial Valley-06	Imperial Valley-06	Imperial Valley-06	Imperial Valley-06
Year	1940	1966	1972	1979	1979	1979	1979
Station Name	Cholame-Shandon Array #5	Managua_ ESSO	Aeropuerto Mexicali	Agrarias	Brawley Airport	Calexico Fire Station	Chihuahua
Magnitude	6.19	6.24	6.53	6.53	6.53	6.53	6.53
Rjb (km)	9.58	3.51	0	0	8.54	10.45	7.29
Rrup (km)	9.58	4.06	0.34	0.65	10.42	10.45	7.29
Vs30 (m/sec)	289.56	288.77	259.86	242.05	208.71	231.23	242.05
ID	RSN170	RSN171	RSN173	RSN178	RSN179	RSN180	RSN181
Earthquake Name	Imperial Valley-06	Imperial Valley-06	Imperial Valley-06	Imperial Valley-06	Imperial Valley-06	Imperial Valley-06	Imperial Valley-06
Year	1979	1979	1979	1979	1979	1979	1979
Station Name	EC County Center FF	EC Meloland Geot. Array	El Centro Array #10	El Centro Array #3	El Centro Array #4	El Centro Array #5	El Centro Array #6
Magnitude	6.53	6.53	6.53	6.53	6.53	6.53	6.53
Rjb (km)	7.31	0.07	8.6	10.79	4.9	1.76	0
Rrup (km)	7.31	0.07	8.6	12.85	7.05	3.95	1.35
Vs30 (m/sec)	192.05	264.57	202.85	162.94	208.91	205.63	203.22
ID	RSN182	RSN183	RSN184	RSN185	RSN265	RSN448	RSN459
Earthquake Name	Imperial Valley-06	Imperial Valley-06	Imperial Valley-06	Imperial Valley-06	Victoria Mexico	Morgan Hill	Morgan Hill
Year	1979	1979	1979	1979	1980	1984	1984
Station Name	El Centro Array #7	El Centro Array #8	Imperial Valley-06	Holtville Post Office	Cerro Priet	Anderson Dam	Gilroy Array #6
Magnitude	6.53	6.53	6.53	6.53	6.33	6.19	6.19
Rjb (km)	0.56	3.86	5.09	5.35	13.8	3.22	9.85
Rrup (km)	0.56	3.86	5.09	7.5	14.37	3.26	9.87
Vs30 (m/sec)	210.51	206.08	202.26	202.89	471.53	488.77	663.31
ID	RSN461	RSN558	RSN723	RSN725	RSN728	RSN821	RSN1101
Earthquake Name	Morgan Hill	Chalfant Valley-02	Superstition Hills02	Superstition Hills02	Superstition Hills02	Erzican Turkey	Kobe Japan
Year	1984	1986	1987	1987	1987	1992	1995
Station Name	Halls Valley	Zack Brothers Ranch	Parachute Test Site	Poe Road (temp)	Westmorland Fire St.	Erzincan	Amagasaki
Magnitude	6.19	6.19	6.54	6.54	6.54	6.69	6.9
Rjb (km)	3.45	6.44	0.95	11.16	13.03	0	11.34
Rrup (km)	3.48	7.58	0.95	11.16	13.03	4.38	11.34
Vs30 (m/sec)	281.61	316.19	348.69	316.64	193.67	352.05	256
ID	RSN1108	RSN1114	RSN2734	RSN3943	RSN3965	RSN4065	RSN4071

Table 3. Ground motion specifications

Earthquake Name	Kobe Japan	Kobe Japan	Chi-Chi_ Taiwan04	Tottori_ Japan	Tottori_ Japan	Parkfield-02_ CA	Parkfield-02_ CA
Year	1995	1995	1999	2000	2000	2004	2004
Station Name	Kobe University	Port Island	CHY074	SMN015	TTR008	Parkfield - EAD.	Parkfield - MID.
Magnitude	6.9	6.9	6.2	6.61	6.61	6	6
Rjb (km)	0.9	3.31	6.02	9.1	6.86	1.37	0.61
Rrup (km)	0.92	3.31	6.2	9.12	6.88	2.85	2.57
Vs30 (m/sec)	1043	198	553.43	616.55	139.21	383.9	397.57
ID	RSN4084	RSN4098	RSN4100	RSN4102	RSN4111	RSN4115	
Earthquake Name	Parkfield-02_ CA	Parkfield-02_ CA	Parkfield-02_ CA	Parkfield-02_ CA	Parkfield-02_ CA	Parkfield-02_ CA	-
Year	2004	2004	2004	2004	2004	2004	-
Station Name	SCHOOL BLDG.	Cholame 1E	Cholame 2WA	Cholame 3W	Fault Zone 7	Fault Zone 12	-
Magnitude	6	6	6	6	6	6	-
Rjb (km)	0.95	1.66	1.63	2.55	0.95	0.88	-
Rrup (km)	2.68	3	3.01	3.63	2.67	2.65	-
Vs30 (m/sec)	269.55	326.64	173.02	230.57	297.46	265.21	-

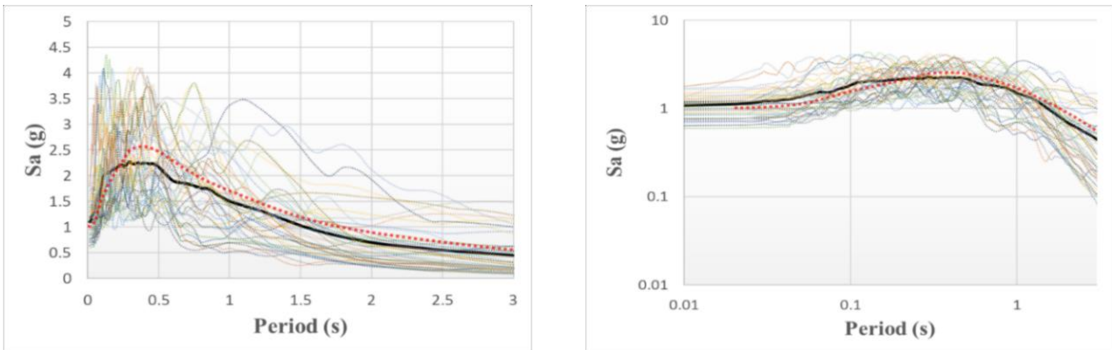

(a) DBE level (b) MCE level

Figure 5. Scaled spectrum of ground motions

utilized CFRP, HCFRP, and steel materials, each possessing distinct mechanical properties, by applying the previously validated material model. The beams and bracing elements were modeled using the steel02 material class, characterized by an elastic modulus of 200 GPa and a yield strength of 345 MPa. The concrete cores were modeled using the concrete01 material class and has a compressive strength of 35 MPa, which captures the compressive behavior of concrete while neglecting its tensile response. All frame members in the structure were modeled using nonlinearBeamColumn elements, which effectively simulate the nonlinear behavior of structural components by both geometric and material nonlinearities. This formulation enables the distribution of plasticity along the length of the members. The cross-sectional properties of each structural member were defined using the fiber section method in OpenSees, and this approach was consistently applied to all member sections, as illustrated in Fig. 4. The beam-column connections were modeled using welds for the outer frame and pins for the inner frame. This configuration ensures that the outer frame to support all loads, while the interior frame contributes solely to gravity load support without participating in lateral load resistance. Furthermore, to simulate rigid diaphragm action at each story level, all nodes at a given story were constrained to a master node located at the center of mass of that story. These constraints were applied to the displacements in both the X and Y directions.

Two types of loads were applied to the structure. First, static loads, consisting of a combination of dead and live loads, were applied based on the tributary area assigned to each node at the floor level to analyze the structure under gravity loading. Following the application of static loads, seismic forces were introduced into the model. To simulate this, a nonlinear time history analysis was performed. A total of 41 pairs of near-fault ground motion records were selected and scaled to represent two seismic hazard levels as specified in ASCE07-22: design basis earthquake (DBE) and maximum considered earthquake (MCE). According to the ASCE7-22 adjustment method, a scale factor of 2.628 was applied for the MCE level. For the DBE level, the adjustment factor is set to 2/3 of the factor used for the MCE level. The specifications of the selected ground motion records with strike-slip mechanism are provided in Table 3, and the scale spectrum of the ground motion is given in Fig. 5. The dotted red line represents the ASCE7-22 MCE spectrum, and the bold black line indicates the average response spectrum of the scaled ground motions.

5. Seismic performance evaluation

To evaluate the seismic performance of frame structures using CFCT and CFHT columns, nonlinear seismic analyses were conducted using 41 recorded ground motions across two seismic hazard levels. Based on the results derived from the nonlinear seismic analysis, statistical evaluations were carried out on key response parameters, including maximum roof displacement, maximum residual story displacement, column stress, and permanent deformation. These statistical analysis results not only characterize the seismic behavior of the structure but also offer insights into the potential damage levels and overall performance of the building.

Fig. 6 presents the maximum roof displacement of each structural system under different seismic hazard levels. The maximum roof displacement serves as an intuitive indicator of a seismic response. The maximum roof displacement limit is specified as 10 times the allowable displacement h (Total height)/500 due to wind load [40]. Structures utilizing CFCT and CFHT columns, which possess higher stiffness, exhibited slightly lower average maximum roof displacements compared to those with CFST columns. As expected, the MCE level, characterized by more frequent and intense ground shaking than the DBE level, resulted in greater structural displacement and damage. Additionally, irrespective of the seismic hazard level, the maximum roof displacement was consistently larger in the X-axis direction than in the Y-axis direction. At the MCE level, the average maximum roof displacements in the X-axis direction were 225.08 mm for CFCT, 219.67 mm for CFHT, and 235.68 mm for CFST. In the Y-axis direction, the corresponding values were 241.01 mm for CFCT, 245.25 mm for CFHT, and 264.45 mm for CFST. At the DBE level, the average maximum roof displacements in the X-axis direction were 124.33 mm for the CFCT structure, CFHT showed 119.72 mm, and CFST showed 135.77 mm, and CFCT showed 124.18 mm, CFHT showed 116.31 mm, and CFST showed 132.39 mm in the

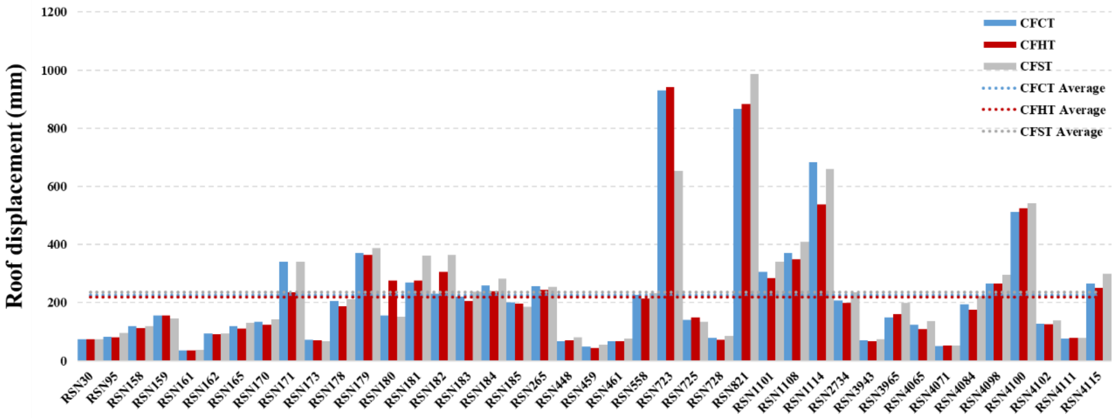

(a) X direction at the MCE level

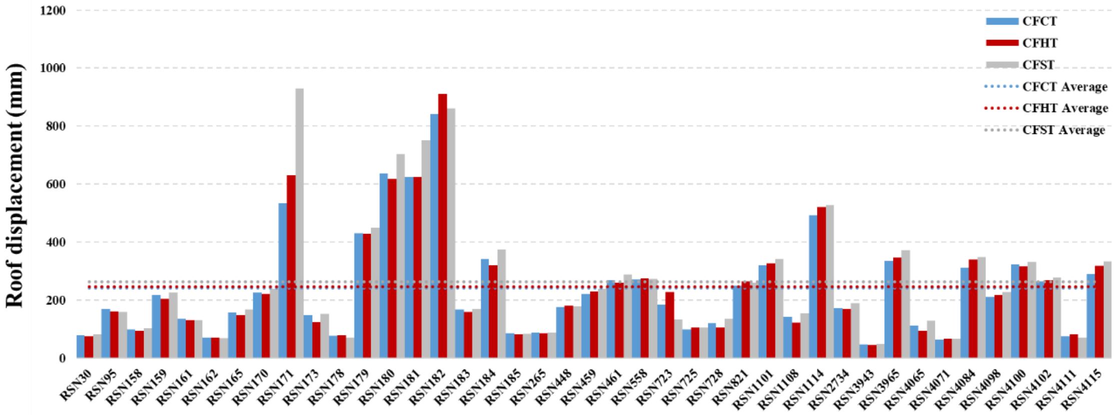

(b) Y direction at the MCE level

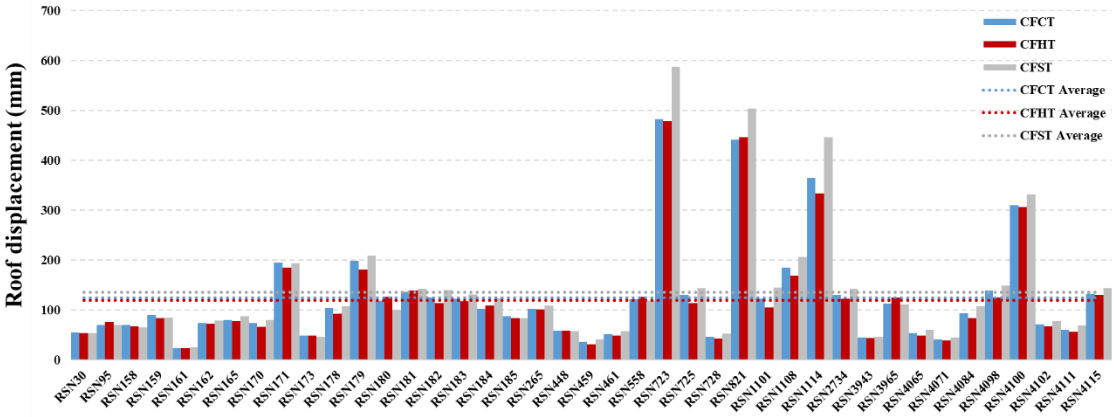

(c) X direction at the DBE level

Figure 6. Maximum roof displacement results (Continued)

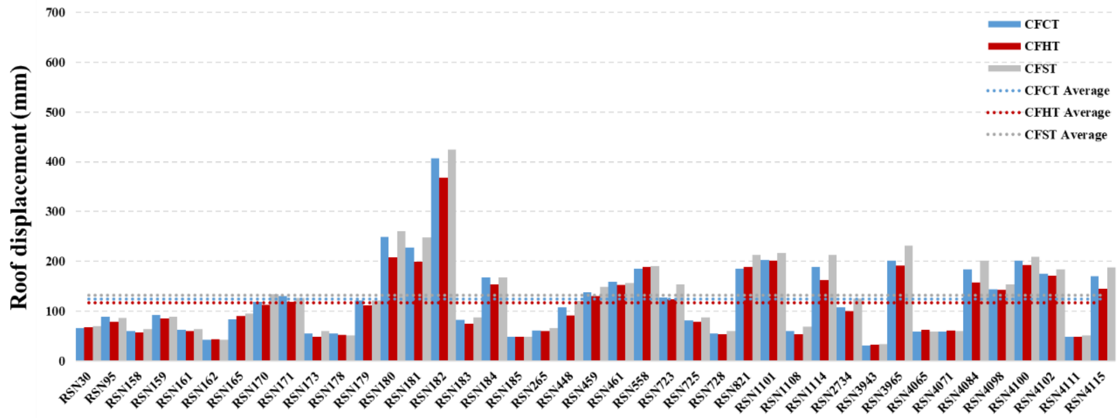

(d) Y direction at the DBE level

Figure 6. Maximum roof displacement results

Y-axis direction. At the MCE level, the largest maximum roof displacement was 986.62 mm, observed in the CFST structure during the RSN821 earthquake, and the smallest displacement at this level was 34.76 mm, recorded in the CFHT structure under the RSN161 earthquake. At the DBE level, the largest maximum roof displacement of 587.08 mm occurred in the CFST structure during the RSN821 earthquake, and the smallest displacement of 23.34 mm occurred in the CFHT structure during the RSN161 earthquake. Some structures showed results exceeding the allowable displacement limit, but on average, CFCT, CFHT, and CFST structures showed results within the allowable displacement limit.

Figs. 7 and 8 present the distribution results of the inter-story drift ratio (ISDR) at the 15.9, 50, and 84.1 percentiles according to seismic hazard levels. Overall, the CFCT and CFHT column structures exhibited lower ISDR values compared to the CFST column structures. The ISDR of the CFST column structures occurs largely on the first floor, but the ISDR of the CFCT and CFHT column structures occur similarly on the first and second floors. Due to the material properties, this behavior is attributed to the CFST column structures transitioning into a plastic state on the first floor, whereas the CFCT and CFHT column structures predominantly maintain elastic behavior. The allowable ISDR limit under seismic loading is specified as 2% [41, 42]. Based on the allowable ISDR limit, the CFCT and CFHT column structures demonstrate, on average, safer performance than the CFST column structures across varying levels of seismic hazard. At the MCE level, the proportion of ground motions resulting in an ISDR equal to the 2% limit was 37% for CFCT, 32% for CFHT, and 46% for CFST at the MCE level, and 5% for CFCT, 6% for CFHT, and 12% for CFST at the DBE level, indicating notable differences among the column types. The ISDR of the 15.9 and 50 percentiles remained within the allowable 2% limit for all structures. However, the ISDR at the 80 percentiles indicated exceedance of the allowable limit under the MCE level, with average values of 2.9% for CFCT in both directions, 2.8% for CFHT, and 3.8% for CFST. At the DBE level, the average of CFCT in both directions was 1.6%, 1.5% for CFHT, and 1.8% for CFST, but the CFST structure exhibited an unsafe result of more than 2% in the Y direction.

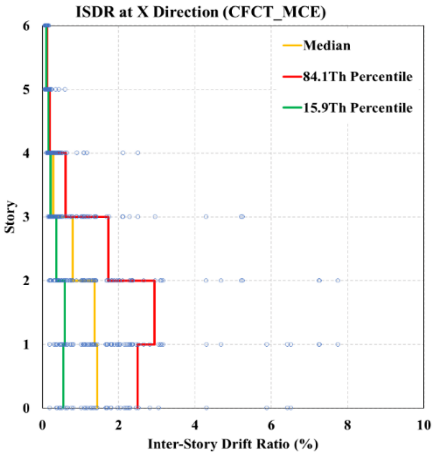

(a) CFCT ISDR in X direction

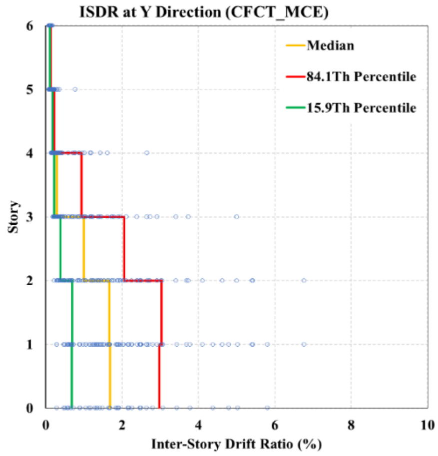

(b) CFCT ISDR in Y direction

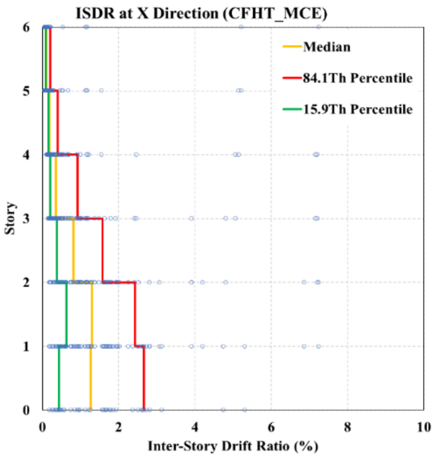

(c) CFHT ISDR in X direction

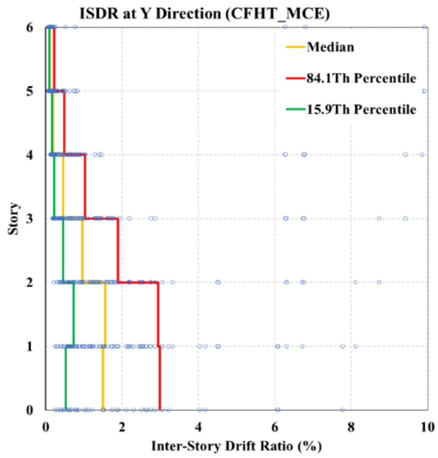

(d) CFHT ISDR in Y direction

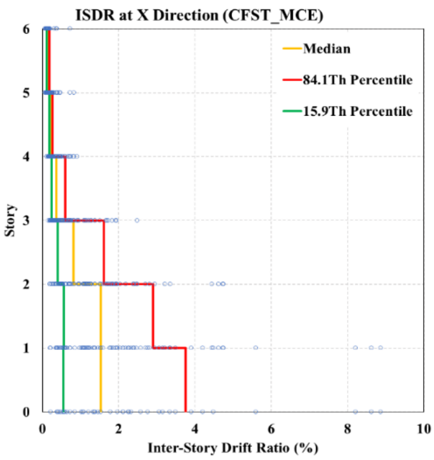

(e) CFST ISDR in X direction

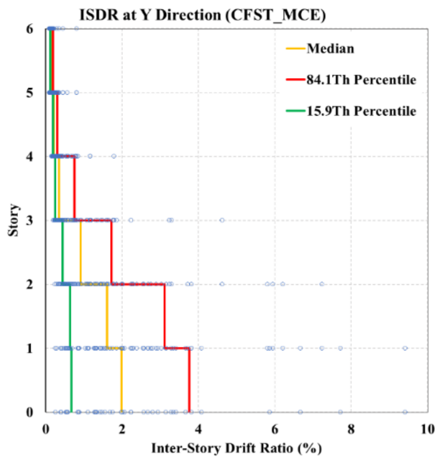

(f) CFST ISDR in Y direction

Figure 7. Inter-story drift ratio results at the MCE level

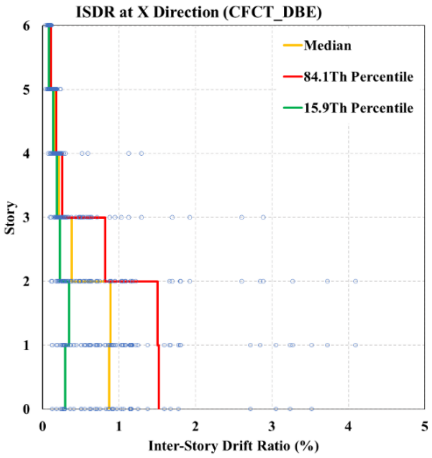

(a) CFCT ISDR in X direction

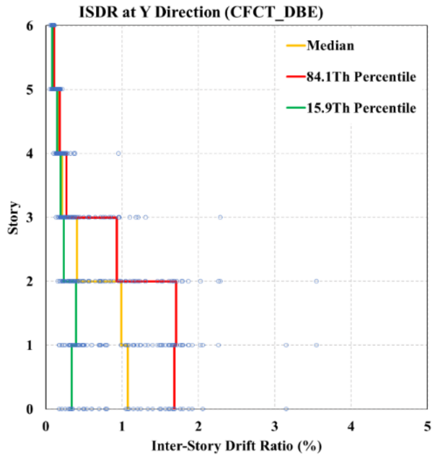

(b) CFCT ISDR in Y direction

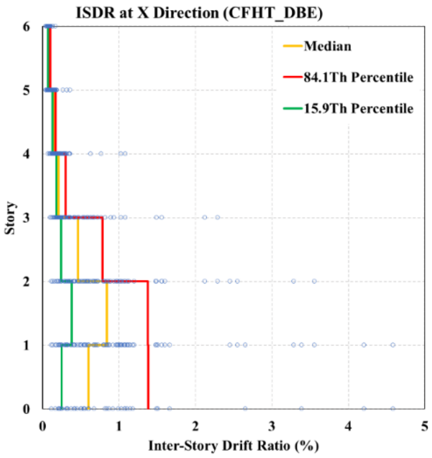

(c) CFHT ISDR in X direction

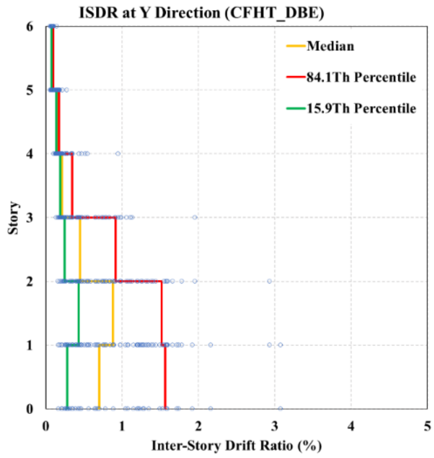

(d) CFHT ISDR in Y direction

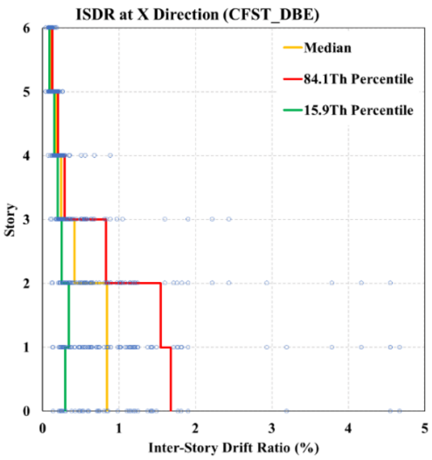

(e) CFST ISDR in X direction

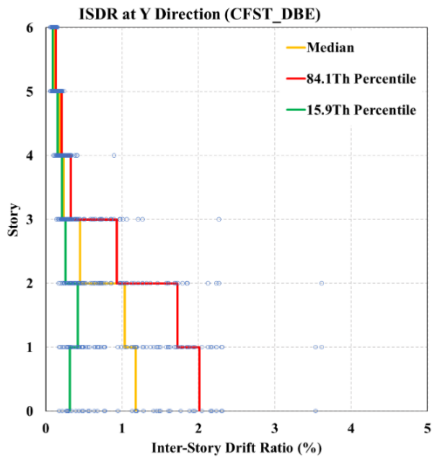

(f) CFST ISDR in Y direction

Figure 8. Inter-story drift ratio results at the DBE level

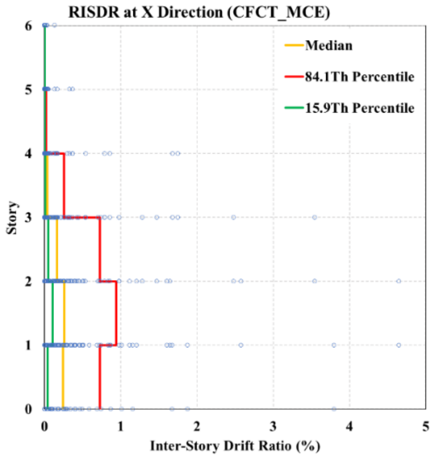

(a) CFCT ISDR in X direction

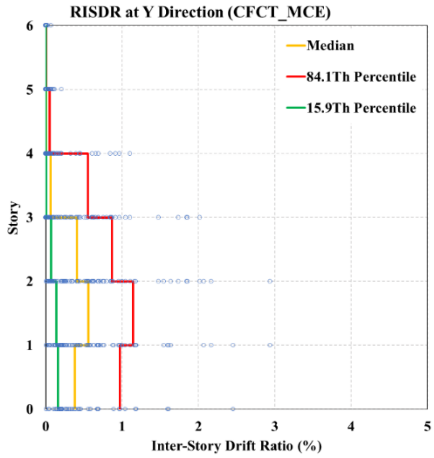

(b) CFCT ISDR in Y direction

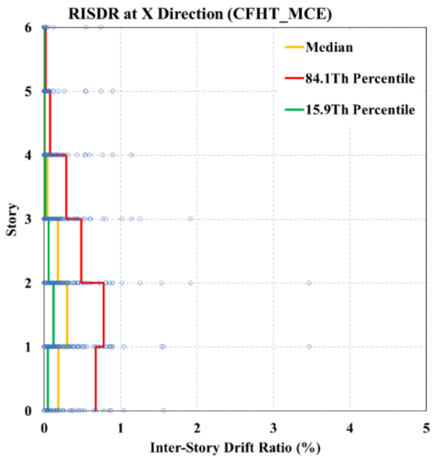

(c) CFHT ISDR in X direction

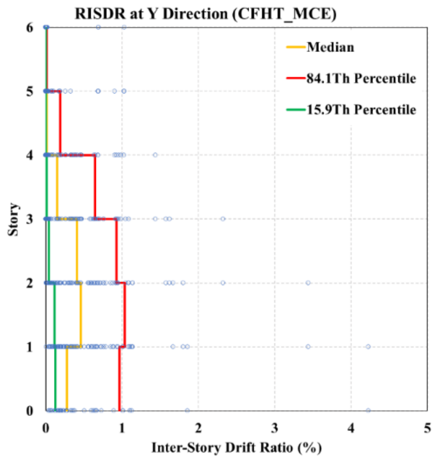

(d) CFHT ISDR in Y direction

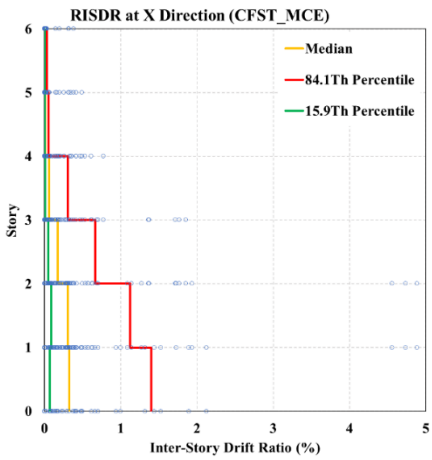

(e) CFST ISDR in X direction

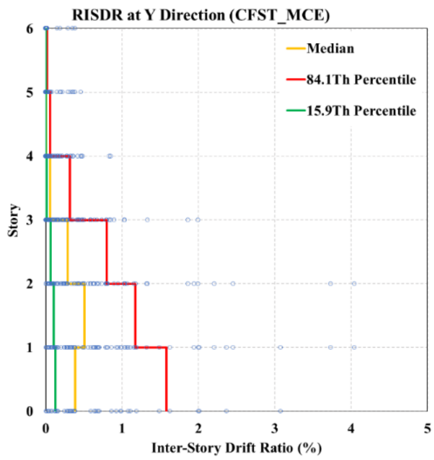

(f) CFST ISDR in Y direction

Figure 9. Residual inter-story drift ratio results at the MCE level

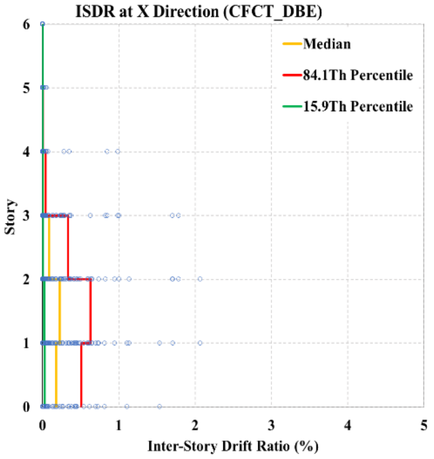

(a) CFCT ISDR in X direction

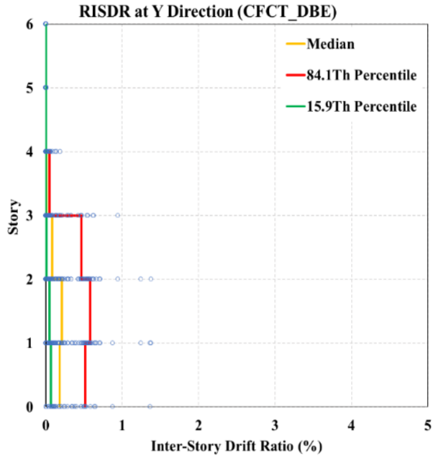

(b) CFCT ISDR in Y direction

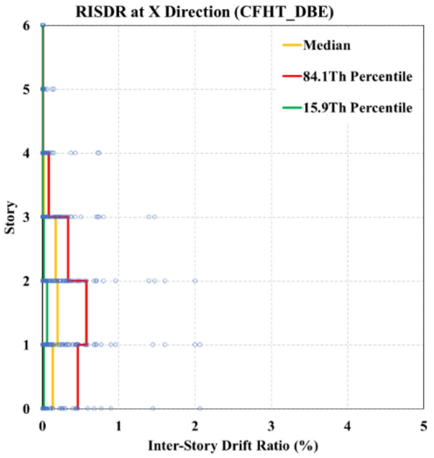

(c) CFHT ISDR in X direction

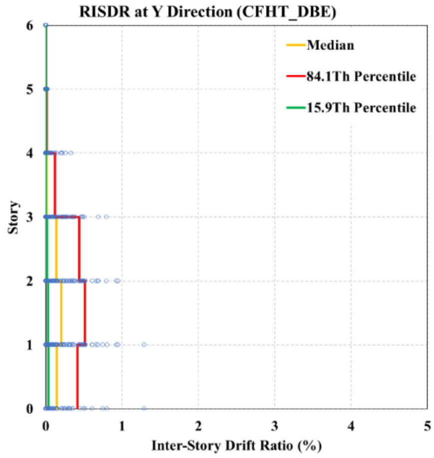

(d) CFHT ISDR in Y direction

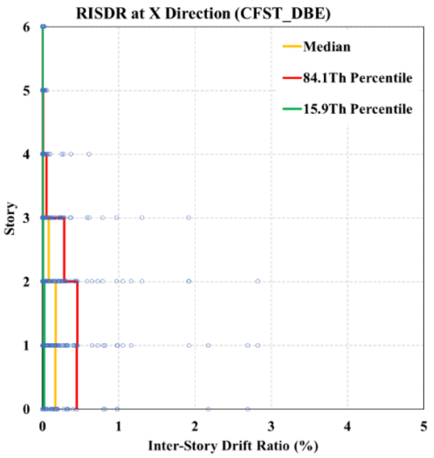

(e) CFST ISDR in X direction

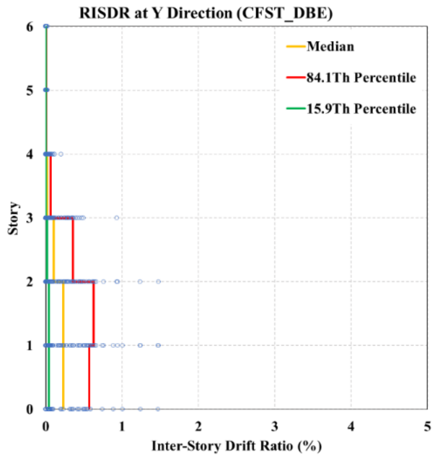

(f) CFST ISDR in Y direction

Figure 10. Residual Inter-story drift ratio results at the DBE level

Figs. 9 and 10 present the distribution results of residual inter-story drift ratio (RISDR) at 15.9, 50, and 84.1 percentiles across varying seismic hazard levels. RISDR serves as a critical indicator of post-earthquake damage in a structure. The two RISDR limits required for determining economic recovery or complete collapse of the structure damage are 0.5% and 1.0%, respectively [43]. If the RISDR exceeds 0.5%, significant repair costs are typically necessary to restore the structure's deformation. When the RISDR surpasses 1.0%, the damage is severe enough to render the structure uninhabitable, resulting in a total loss of the structure. The CFCT and CFHT column structures showed lower RISDR values than the CFST column structures. The RISDR in CFST column structures predominantly occurs on the first floor, leading to permanent deformation caused by plastic hinge formation in the first-floor columns. In contrast, the RISDR of CFCT and CFHT column structures is mainly observed on the second floor, where the columns generally remain in an elastic state. Considering the allowable RISDR limit, CFCT and CFHT column structures demonstrate safer performance on average compared to CFST columns across various seismic risk levels. The ground motions showing a RISDR of 1% or more were 19% for CFCT, 18% for CFHT, and 26% for CFST at the MCE level, and 6% for CFCT, 3% for CFHT, and 8% for CFST at the DBE level, showing some differences. Additionally, the RISDR at the 15.9th and 50th percentiles remained below 1% on average in both directions, indicating safe performance regardless of the seismic risk level. At the 80th percentile, the RISDR values at the MCE level were 1.0% for CFCT, 0.9% for CFHT, and 1.5% for CFST in both directions, indicating the need for repair or damage. At the DBE level, the bidirectional average CFCT was 0.6%, CFHT was 0.5%, and CFST was 0.6%, suggesting maintenance is required.

Figs. 11, 12 and 13 present the stress, energy dissipation amount and permanent deformation observed in the CFRP, HCFRP, and Steel tube components of the lower left column in the structural layout. Column stress and energy dissipation amount are key indicator of the capacity of a column, which is the primary structural member of the building, to withstand seismic loads while remaining intact and dissipating earthquake energy. Additionally, permanent deformation serves as an indicator of the extent of damage sustained by the column owing to seismic activity. The column stresses and energy dissipation amounts observed in the CFCT and CFHT columns were higher than those recorded in the CFST columns. In particular, the maximum column stress underground motion was 984.88 MPa for the CFCT column at the MCE level, which was 1.67 times greater than that of the CFHT column and 5.48 times greater than that of the CFST column. At the DBE level, the CFCT column exhibited maximum stress of 477.30 MPa, again 1.67 times higher than that of the CFHT columns and 5.48 times higher than the CFST column. The average column stress was 410.15 MPa for CFCT, 196.74 MPa for CFHT, and 129.50 MPa for CFST at the MCE level, and 281.48 MPa for CFCT, 195.98 MPa for CFHT, and 117.45 MPa for CFST at the DBE level. In addition, the average energy dissipation amount was 9.16 J/mm^3 for CFCT, 8.68 J/mm^3 for CFHT, and 6.53 J/mm^3 for CFST at the MCE level, and 4.91 J/mm^3 for CFCT, 4.64 J/mm^3 for CFHT, and 4.17 J/mm^3 for CFST at the DBE level. These results suggest that CFCT columns demonstrate superior seismic performance compared to CFHT and CFST columns because they dissipate more seismic energy. The permanent strain in the CFCT and CFHT columns was lower than that in the CFST columns. This indicates that CFCT columns not only dissipate seismic energy more effectively than CFHT and CFST columns but also exhibit elastic behavior under seismic loading. At the MCE level, the average permanent strain was 0.0016 mm/mm for CFCT, 0.0020 mm/mm for CFHT, and 0.0039 mm/mm for CFST. At the DBE level, the average values were 0.0008 mm/mm for CFCT, 0.0009 mm/mm for CFHT, and 0.0011 mm/mm for CFST.

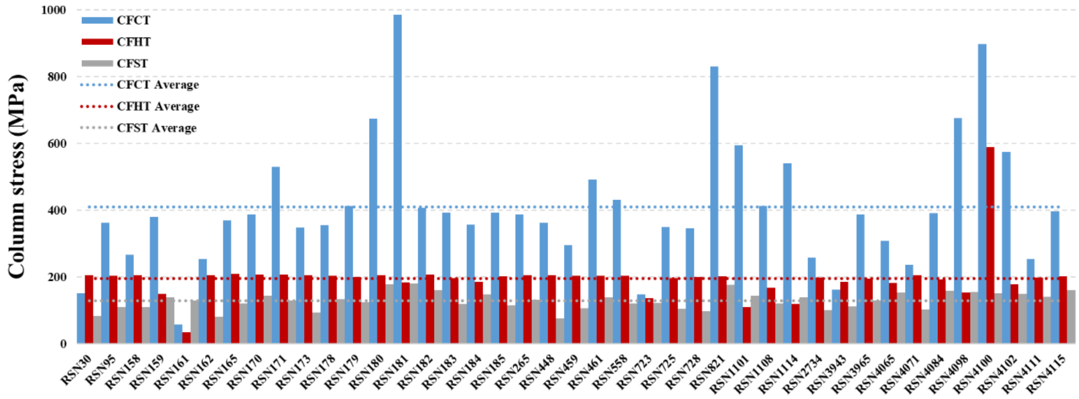

(a) MCE level

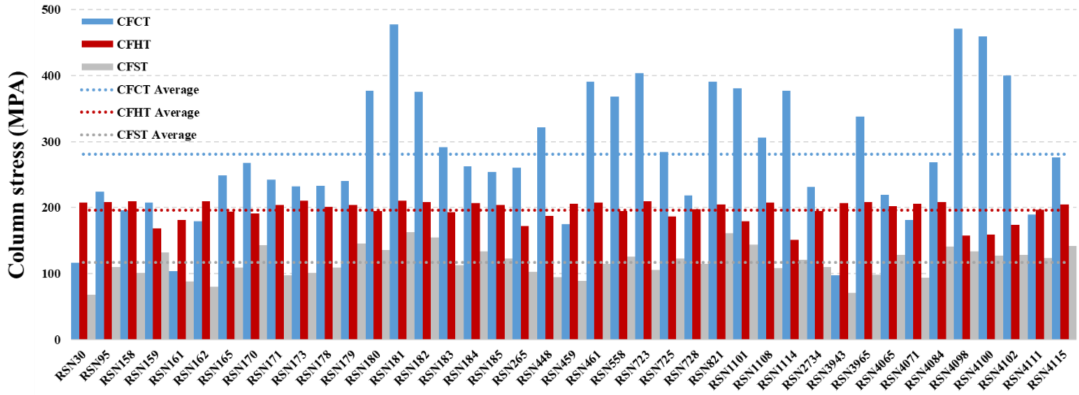

(b) DBE level

Figure 11. Column stress results

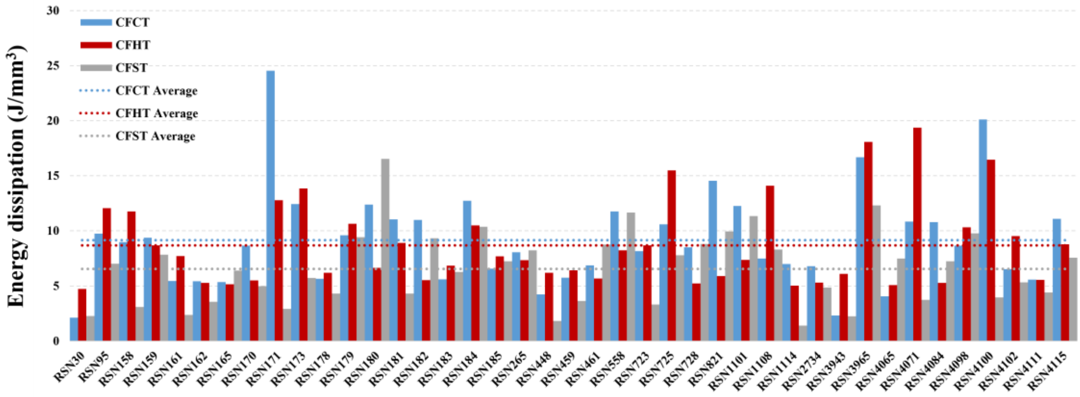

(a) MCE level

Figure 12. Energy dissipation amount results (Continued)

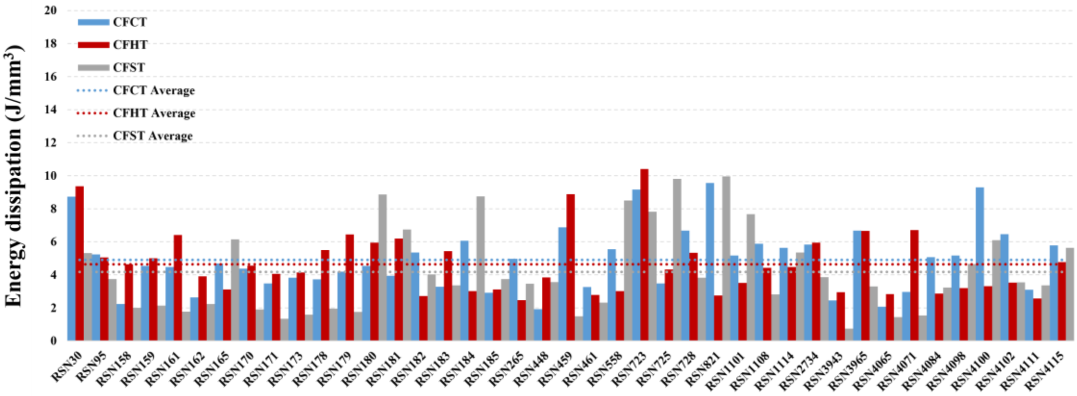

(b) DBE level

Figure 12. Energy dissipation amount results

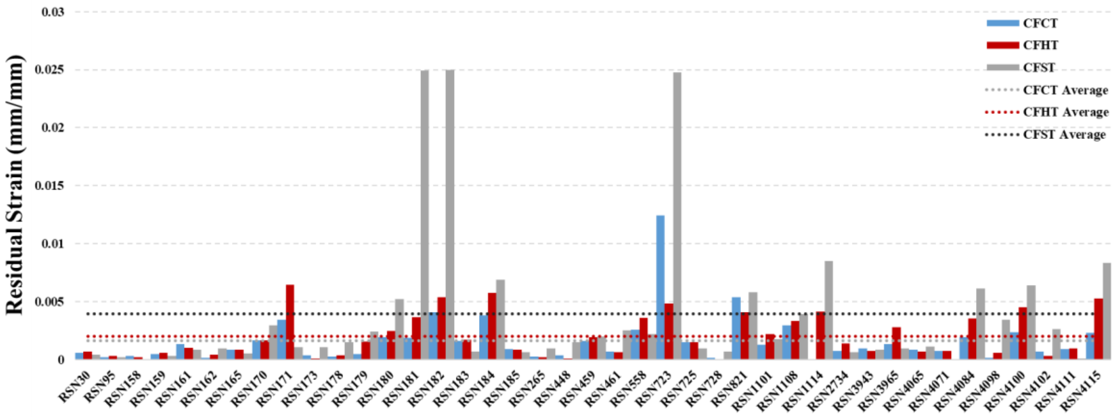

(a) MCE level

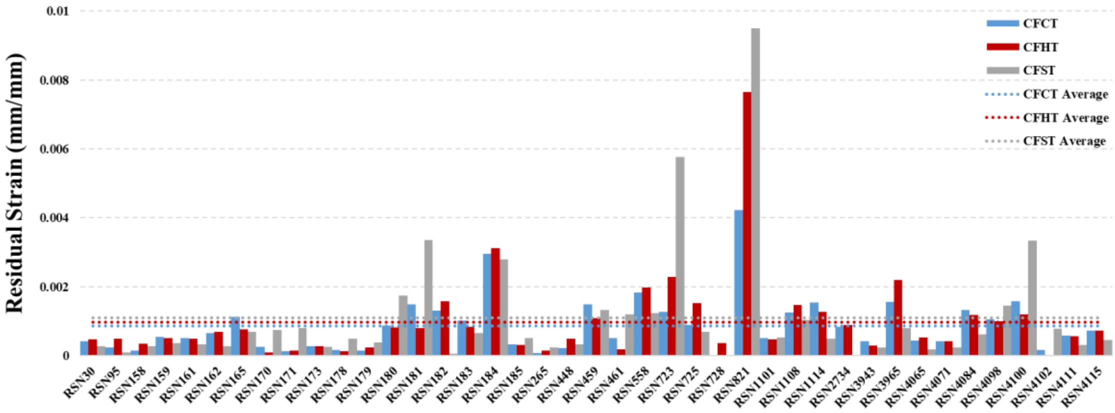

(b) DBE level

Figure 13. Permanent deformation results

6. Conclusions

In this study, the seismic performance of CFT column structures using CFRP and HCFRP was evaluated. Tensile and compressive cyclic material tests were conducted on CFRP and HCFRP to obtain behavioral characteristics, which were then simulated using the OpenSees program. The detailed design of a six-story building structure was completed, and numerical models with CFCT, CFHT, and CFST columns were developed. Furthermore, numerical analyses were performed by applying 41 ground motions based on seismic risk, and seismic performance was evaluated in terms of maximum roof displacement, story displacement ratio, residual story displacement ratio, and column stress. Based on the numerical analysis, the following conclusions are drawn.

(1) First, a simulation study was conducted to model the material behavior of CFRP and HCFRP, which are central to this study. The OpenSees analysis results showed an error of less than 0.5% compared to test results, indicating that the result is reliable for structural numerical analysis.

(2) Numerical analysis was conducted on building structures with CFCT, CFHT, and CFST columns according to seismic risk levels. In terms of maximum roof displacement, the superior performance of CFRP and HCFRP was clearly demonstrated. The average maximum roof displacement for CFCT and CFHT columns was 7% lower than that of CFST columns at the MCE level and 11% lower at the DBE level. Consequently, since the maximum roof displacement was smaller in the CFCT and CFHT column structures compared to the CFST column structures, it is expected that the structural damage would be reduced.

(3) Regarding the ISDR and RISDR that occurred on each floor of the building structure, the CFCT and CFHT column structures exhibited smaller values compared to the CFST column structures. In addition, based on the allowable limits for ISDR and RISDR, the CFCT and CFHT column structures demonstrated safer results on average than the CFST column across varying seismic risk levels. Specifically, the ISDR exceeded the limit criteria 12% more frequently at the MCE level and 7% more frequently at the DBE level for CFST columns compared to CFCT and CFHT columns. Similarly, the RISDR exceeded the limit criteria 8% more often at the MCE level and 4% more often at the DBE level for CFST columns than for CFCT and CFHT columns.

(4) Based on the results of column stress, energy dissipation amount and permanent strain, CFCT and CFHT column structures demonstrate superior seismic performance compared to CFST column structures, primarily owing to their enhanced capacity to dissipate seismic energy. In addition, CFCT and CFHT columns are expected to exhibit better elastic behavior than CFST columns. The average column stress was 2.1 and 1.5 times higher for CFCT and CFHT columns, respectively, at the MCE level, 2.4 and 1.4 times higher for CFST columns, respectively. The average energy dissipation amount was 1.4 and 1.3 times higher for CFCT and CFHT columns, respectively, at the MCE level, 1.1 times higher for CFST columns, respectively. In addition, the average permanent strain was 0.4 and 0.5 times higher for CFST columns at the MCE level, and 0.8 and 0.9 times higher for CFCT and CFHT columns, respectively. Therefore, it is considered that CFCT and CFHT columns can be used as replacements for conventional CFST columns depending on requirements and performance.

Acknowledgements

This research was supported by Basic Science Research Program through the National Research Foundation of Korea (NRF) funded by the Ministry of Education (grant number: RS-

2023-00248140).

References

1. Wu, N., Tan, K. H., (2023). Testing, modelling and design of concentrically-loaded concrete-encased concrete-filled steel tube slender column. Journal of Constructional Steel Research, 203, 107810. https://doi.org/10.1016/j.jcsr.2023.107810
2. Gao, B., Xu, L., Huang, L., Chi, Y., Yu, M., Wen, S., (2024). Seismic performance of a novel concrete-filled steel tube column to continuous reinforced concrete beam joint with multiple openings in the core region. Engineering Structures, 319, 118775. https://doi.org/10.1016/j.engstruct.2024.118775
3. Mortazavi, S. J., Mansouri, I., Farzampour, A., Retzepis, E., Hu, J. W., (2024). Evaluation of the Fire Behavior of Low-Rise Eccentrically Braced Frame Structures Under Different Fire Scenarios. Fire Technology, 60, 3499–3528. https://doi.org/10.1007/s10694-024-01587-9
4. Song, T. Y., Yu, W. C., Xiang, K., Zhou, H. Y., (2022). Critical temperatures of concrete-filled steel tubular columns for early-warning of fire-induced failure. Journal of Constructional Steel Research, 191, 107190. https://doi.org/10.1016/j.jcsr.2022.107190
5. Al-Rousan, R. Z., (2022). Cyclic lateral behavior of NLFEA heat-damaged circular CFT steel columns confined at the end with CFRP composites. Case Studies in Construction Materials, 17, e01223. https://doi.org/10.1016/j.cscm.2022.e01223
6. Al-Rousan, R. Z., (2021). Impact of elevated temperature and anchored grooves on the shear behavior of reinforced concrete beams strengthened with CFRP composites. Case Studies in Construction Materials, 14(1), e00487. https://doi.org/10.1016/j.cscm.2021.e00487
7. Li, G., Hou, C., Shen, L., (2021). Life-cycle analysis of FRP-strengthened offshore CFST columns suffering from steel corrosion. Composite Structures, 277, 114607. https://doi.org/10.1016/j.compstruct.2021.114607
8. Lin, S., Li, Z., Zhao, Y. G., (2023). Behavior of eccentrically loaded circular concrete-filled steel tube stub columns with localized corrosion. Composite Structures, 288, 116227. https://doi.org/10.1016/j.engstruct.2023.116227
9. Zeng, W., Ayough, P., Wang, Y. H., Elchalakani, M., (2024). Numerical simulation of axially loaded circular concrete-filled steel tubular short columns with localized corrosion. Engineering Structures, 312, 118243. https://doi.org/10.1016/j.engstruct.2024.118243
10. Li, H., Li, M., Guo, W., Zhao, Q., Zhang, H., (2025). Bond behavior between steel and solid waste concrete activated by soda residue and carbide slag in concrete-filled steel tubes (CFSTs). Case Studies in Construction Materials, 22, e04383. https://doi.org/10.1016/j.cscm.2025.e04383
11. Liu, S., Wang, X., Li, Y., Liu, Y., (2024). Stress-strain relationship of airfoiled-shaped milled-cut steel fiber-reinforced concrete under uniaxial compression: Experiments and analytical model. Case Studies in Construction Materials, 21, e03925. https://doi.org/10.1016/j.cscm.2024.e03925
12. Wang, Z., Han, J., Wei, J., Lu, J., Li, J., (2022). The axial compression mechanical properties and factors influencing spiral-ribbed thin-walled square concrete-filled steel tube composite members. Case Studies in Construction Materials, 17, e01510. https://doi.org/10.1016/j.cscm.2022.e01510
13. Mortazavi, S. J., Mansouri, I., Awoyera, P. O., Hu, J. W., (2022), Comparison of thermal performance of steel moment and eccentrically braced frames. Journal of Building Engineering, 49, 104052. https://doi.org/10.1016/j.jobe.2022.104052
14. Ma, Y., Ma, K., Han, Xiao., Yao, T., (2023). Experimental investigation of FRP-confined HSC-filled steel tube stub columns under axial compression. Engineering Structures, 208, 115670. https://doi.org/10.1016/j.engstruct.2023.115670
15. Zhang, S., Miao, K., Xu, X., Luo, B., Shi, W., (2023). Experimental and Theoretical Study of Concrete-Filled Steel Tube Columns Strengthened by FRP/Steel Strips Under Axial Compression. International Journal of Concrete Structures and Materials, 17(1). https://doi.org/10.1186/s40069-022-00556-2

16. Wang, C., Liang, J., Li, W., He, C., (2023). Axial compression performance of square concrete filled double skin SHS steel tubular columns confined by CFRP. Scientific Reports, 13, 10075. https://doi.org/10.1038/s41598-023-37101-4
17. Ilki, A., Peker, O., Karamuk, E., Demir, C., Kumbasar, N., (2008). FRP retrofit of low and medium strength circular and rectangular reinforced concrete columns. Journal of Materials in Civil Engineering, 20(2), 169-188. https://doi.org/10.1061/%28ASCE%290899-1561%282008%2920%3A2%28169%29
18. Wei, Y. Y., Wu, Y. F., (2012). Unified stress-strain model of concrete for FRP-confined columns. Construction and Building Materials, 26(1), 381-392. https://doi.org/10.1016/j.conbuildmat.2011.06.037
19. Yazici, V., Hadi, M. N. S., (2012). Normalized Confinement Stiffness Approach for Modeling FRP-Confined Concrete. Journal of Composites for Construction, 16(5), 520-528. https://doi.org/10.1061/%28ASCE%29CC.1943-5614.0000283
20. Mohamed, H. M., Masmoudi, R., (2010). Axial Load Capacity of Concrete-Filled FRP Tube Columns: Experimental versus Theoretical Predictions. Journal of Composites for Construction, 14(2), 231-243. https://doi.org/10.1061/(ASCE)CC.1943-5614.0000066
21. Ozbakkaloglu, T., (2013a). Axial Compressive Behavior of Square and Rectangular High-Strength Concrete-Filled FRP Tubes. Journal of Composites for Construction, 17(1), 151-161. https://doi.org/10.1061/(ASCE)CC.1943-5614.0000066
22. Ozbakkaloglu, T., (2013b). Compressive behavior of concrete-filled FRP tube columns: Assessment of critical column parameters. Engineering Structures, 51, 188-199. https://doi.org/10.1016/j.engstruct.2013.01.017
23. Xu, Y., Liu, C., Chai, L., Luo, C., (2019). The effect of defect size on the integrity of CFRP-confined concrete column. Construction and Building Materials, 200, 521-529. https://doi.org/10.1016/j.conbuildmat.2018.12.087
24. Bae, Y. J., Sim, V., Lee, S. M., Jung, W. Y., (2025). Fatigue performance criteria for CFRP Reinforcements Based on RC behavior in civil construction. Journal of Asian Architecture and Building Engineering, 24(6), 5257-5271. https://doi.org/10.1080/13467581.2024.2421230
25. Sadeghian, P., Rahai, A. R., Ehsani, M. R., (2010). Effect of Fiber Orientation on Compressive Behavior of CFRP-confined Concrete Columns. Journal of Reinforced Plastics and Composites, 29(9), 1335-1346. https://doi.org/10.1177/0731684409102985
26. Vincent, T., Ozbakkaloglu, T., (2013). Influence of fiber orientation and specimen end condition on axial compressive behavior of FRP-confined concrete. Construction and Building Materials, 47, 814-826. https://doi.org/10.1016/j.conbuildmat.2013.05.085
27. Hain, A., Motaref, S., Zaghi, A. E., (2019). Influence of fiber orientation and shell thickness on the axial compressive behavior of concrete-filled fiber-reinforced polymer tubes. Construction and Building Materials, 220, 353-363. https://doi.org/10.1016/j.conbuildmat.2019.05.194
28. Nisticò, N., Monti, G., (2013). RC square sections confined by FRP: Analytical prediction of peak strength. Composites Part B-Engineering, 45(1), 127-137. https://doi.org/10.1016/j.compositesb.2012.09.041
29. Marí, R., Oller, E., Bairán, J. M., (2011). Predicting the Response of FRP-Strengthened Reinforced-Concrete Flexural Members with Nonlinear Evolutive Analysis Models. Journal of Composites for Construction, 15(5), 799-809. https://doi.org/10.1061/(ASCE)CC.1943-5614.0000214
30. Kim, H. S., Jung, B. K., Hu, J. W., (2024). Comparison of Material Performance through Experiments between CFRP and CFRP Hybrid and Steel, Journal of the Korean Society for Advanced Composite Structures, 15(4), 1-8. https://doi.org/10.11004/kosacs.2024.15.4.001
31. ASTM D3039/D3039M (2007). Standard Test Method for Tensile Properties of Polymer Matrix Composite Materials. American Society for Testing and Materials, West Conshohocken, PA, USA.
32. ASTM D6641/D6641M (2007), Standard Test Method for Compressive Properties of Polymer Matrix Composite Materials Using a Combined Loading Compression (CLC) Test Fixture, American Society for Testing and Materials, West Conshohocken, PA, USA.
33. McKenna, F., Scott, M. H., Fenves, G. L., (2010). Nonlinear Finite-Element Analysis Software Architecture Using Object Composition. Journal of Computing in Civil Engineering, 24(1), 95-107.

https://doi.org/10.1061/(ASCE)CP.1943-5487.0000002
34. McKenna, F., (2011). OpenSees: A Framework for Earthquake Engineering Simulation. Computing in Science & Engineering, 13(4), 58-66. https://doi.org/10.1109/MCSE.2011.66
35. Mansouri, I., Mortazavi, S. J., Manfredi, M., Awoyera, P. O., Mansouri, E., Khaki, A., Hu, J. W., (2023). Development of New Material Models for Thermal Behavior of Cold-Formed G-450 and G-550 Steels in OpenSees Software. Journal of Architectural Engineering, 29(2). https://doi.org/10.1061/JAEIED.AEENG-1491
36. Mortazavi, S. J., Mansouri, I., Awoyera, P. O., Hu, J. W., (2022). Comparison of thermal performance of steel moment and eccentrically braced frames. Journal of Building Engineering, 49. https://doi.org/10.1016/j.jobe.2022.104052
37. ANSI/AISC 341-22 (2022). Seismic Provisions for Structural Steel Buildings, American Institute of Steel Construction, Chicago, IL, USA.
38. ANSI/AISC 360-22 (2023). Specification for Structural Steel Buildings, American Institute of Steel Construction, Chicago, IL, USA.
39. ASCE/SEI 7-22 (2022). Minimum Design Loads and Associated Criteria for Buildings and Other Structures, American Society of Civil Engineers, 1801 Alexander Bell Drive Reston, VA, USA.
40. ASCE/SEI 7-16 (2018). Minimum Design Loads and Associated Criteria for Buildings and Other Structures, American Society of Civil Engineers, 1801 Alexander Bell Drive Reston, VA, USA.
41. ASCE/SEI 7-05 (2006). Minimum Design Loads for Buildings and Other Structures, American Society of Civil Engineers, 1801 Alexander Bell Drive Reston, VA, USA.
42. Ban, W. H., Hu, J. W., Ju, Y. H., (2020). Seismic performance evaluation of recentering braced frame structures using superelastic shape memory alloys-nonlinear dynamic analysis, J. Korean Soc. Civ. Eng. 40(4), 353–362. https://doi.org/10.12652/Ksce.2020.40.4.0353
43. Richards, P. W., McCall, A. J., Marshall, J. D., (2023). Functional Recovery of Steel Special Moment Frames. Journal of Structural Engineering, 149(3). https://doi.org/10.1061/JSENDH.STENG-11567